Chemical Engineering Journal 536 (2026) 175881

Contents lists available at ScienceDirect

Chemical Engineering Journal

journal homepage: www.elsevier.com/locate/cej

Reverse aging of fully relaxed metallic glasses via ultrasonic vibration loading for enhanced catalytic performance

Shenghao Zeng [a,b], Wenqing Ruan [b,*], Jianyu Chen [b], Zhe Chen [b], Jihan Jiang [b], Xiaodi Liu [b], Qing Chen [c], Shuai Ren [b,*], Xiong Liang [b,*], Jiang Ma [b,*]

[a] Wuhan National High Magnetic Field Center and School of Physics, Huazhong University of Science and Technology, Wuhan, 430074, China
[b] Shenzhen Key Laboratory of High Performance Nontraditional Manufacturing, College of Mechatronics and Control Engineering, Shenzhen University, Shenzhen, 518060, China
[c] Department of Mechanical and Aerospace Engineering, The Hong Kong, University of Science and Technology, Clear Water Bay, Kowloon, Hong Kong, China

ARTICLE INFO

Keywords:
Metallic glasses
Hydrogen evolution reaction
Ultrasonic vibration loading
Aging

ABSTRACT

Metallic glasses (MGs), as distinctive amorphous metallic alloys, exhibit high-density undercoordinated sites and elevated Gibbs free energy, rendering them highly promising candidates for electrocatalysis. However, MGs inevitably undergo aging or structural relaxation over time, which inevitably triggers the degradation of their intrinsic catalytic properties. Consequently, reversing the aging effect of fully relaxed MGs to recover and even boost their catalytic performance has long remained a formidable and unresolved challenge in the field, given that conventional strategies are ineffective in reactivating the relaxed atomic configurations and restoring the high-energy state of MGs. Herein, we report an innovative energy modulation strategy—Ultrasonic Vibration Loading (UV loading). This strategy not only retrieves the energy of fully relaxed MGs but also induces the formation of a biphase structure with coexisting amorphous and crystalline phases, where the synergistic coupling of the crystalline phase's superior electrical conductivity and the amorphous phase's abundant unsaturated coordination sites optimizes the hydrogen adsorption Gibbs free energy to be closer to 0 eV, thereby remarkably enhancing their catalytic performance. The general applicability of this approach is validated by the superior hydrogen evolution reaction (HER) activity of Pt-based MGs and Pd-based MGs in alkaline electrolytes. Our findings underscore the unique merits of UV loading in tailoring the surface energy and catalytic performance of MGs and provide a versatile paradigm for surface energy modulation of advanced electrocatalysts.

1. Introduction

Metallic glasses (MGs), as distinctive amorphous metallic alloys, exhibit a suite of thermodynamic, kinetic, mechanical, and magnetic properties that are absent in crystalline alloys, offering tremendous application prospects in fields ranging from electrocatalysis to energy storage and structural engineering. [1–4] Notably, their highly active surfaces, dense dangling bonds, and undercoordinated active sites—coupled with excellent stability in acidic/alkaline environments and the inducible increase in active sites via electrochemical dealloying—have positioned MGs as a focal material in electrocatalysis research. [5–10] For instance, Pt-based MGs have demonstrated superior performance in the hydrogen evolution reaction (HER), [11–14] while Ni-based MGs exhibit notable advantages in the oxygen evolution reaction (OER). [15–17]

The catalytic efficacy of MGs is governed by two key factors: the density of active sites and the surface energy. Conventional strategies for enhancing the activity of crystalline catalysts—such as modulating chemical composition or defect structure—are largely ineffective for MGs, owing to their inherently homogeneous and disordered atomic structure, which limits adaptability to diverse practical demands. [18–20] In contrast, tailoring the surface energy of MGs—particularly by increasing the density of low-coordination sites (typically located at steps, edges, and kinks, the core active centers for catalytic reactions [21,22])—has emerged as a viable approach to boost catalytic activity. [23–26] The high-energy state and abundant potential active sites of as-cast MGs are partially rooted in their high enthalpy and specific volume, which arise from the rapid-quenching technique used in their synthesis. [8,27,28] These intrinsic characteristics endow MGs with superior catalytic performance, attributed to reduced activation energy and a high

* Corresponding authors.
E-mail addresses: ruanwq@szu.edu.cn (W. Ruan), ren.shuai@ylab.ac.cn (S. Ren), xliang@szu.edu.cn (X. Liang), majiang@szu.edu.cn (J. Ma).

https://doi.org/10.1016/j.cej.2026.175881
Received 25 January 2026; Received in revised form 24 March 2026; Accepted 3 April 2026
Available online 3 April 2026

density of accessible active sites. [29,30]

As metastable materials, MGs inevitably undergo structural relaxation over time—a time-dependent process termed "aging" that originates from the intrinsic thermodynamic metastability of amorphous systems, driving the initial high-energy state toward a more stable configuration. [31,32] Although relaxation primarily occurs at the local structural level, it triggers pronounced degradation of macroscopic properties, including catalytic activity [33,34]. Current efforts to modulate the energy state of MGs have focused on modified processing routes, such as accelerated quenching, [35] elastic loading, [36–38] low-temperature thermal cycling, [39,40] ion irradiation, [41] and severe plastic deformation. [42–45] However, these methods suffer from two critical limitations: high complexity and substantial energy consumption, which have hampered their widespread practical implementation; more importantly, they fail to restore fully relaxed MGs to their original high-energy state. Thus, reversing aging to revitalize the energy state and catalytic performance of fully relaxed MGs remains a formidable challenge in the field.

Recent studies have demonstrated that ultrasonic vibration (UV) loading can induce substantial energy elevation in aged, low-energy MGs—even surpassing that of as-cast counterparts—positioning UV loading as a highly efficient energy enhancement strategy. [2,46–51] Despite this promise, the effect of UV loading on the catalytic performance of MGs—especially fully relaxed MGs—has not been systematically investigated. A comprehensive demonstration of UV loading induced catalytic enhancement in this context would open new avenues for advancing MG-based electrocatalysts.

Herein, we report that UV loading achieves rapid aging reversal in fully aged MGs, thereby achieving a remarkable enhancement in their catalytic performance. Experimental results in alkaline electrolytes show that the catalytic performance of aged MGs (denoted as T_g-**n**h, where $\boldsymbol{n}$ = 1, 3, 5 h) subjected to single-step annealing is degraded relative to the pristine Pt-based MGs (as-cast). In stark contrast, UV loading MGs (UV**m**J-T_g, where **m** = 25, 50, 75 J) exhibit dramatically enhanced catalytic activity compared to the T_g-3 h sample (a model of fully relaxed MGs): the overpotential is reduced by 48%, and the specific activity (SA) is increased by 589%. Furthermore, the UV loading strategy exhibits exceptional general applicability, being effective for both Pt-based and Pd-based MGs. These findings highlight the unique merits of UV loading in tailoring the surface energy and catalytic performance of MGs, while providing a versatile paradigm for surface energy modulation of advanced electrocatalysts.

2. Results and discussion

2.1. Properties evolution in MGs annealed at T_g with varied annealing durations

The high-resolution transmission electron microscopy (HRTEM) image of the as-cast sample (Fig. 1a) distinctly illustrates the homogeneous amorphous microstructure characteristic of MGs. The corresponding selected-area electron diffraction (SAED) patterns corroborate

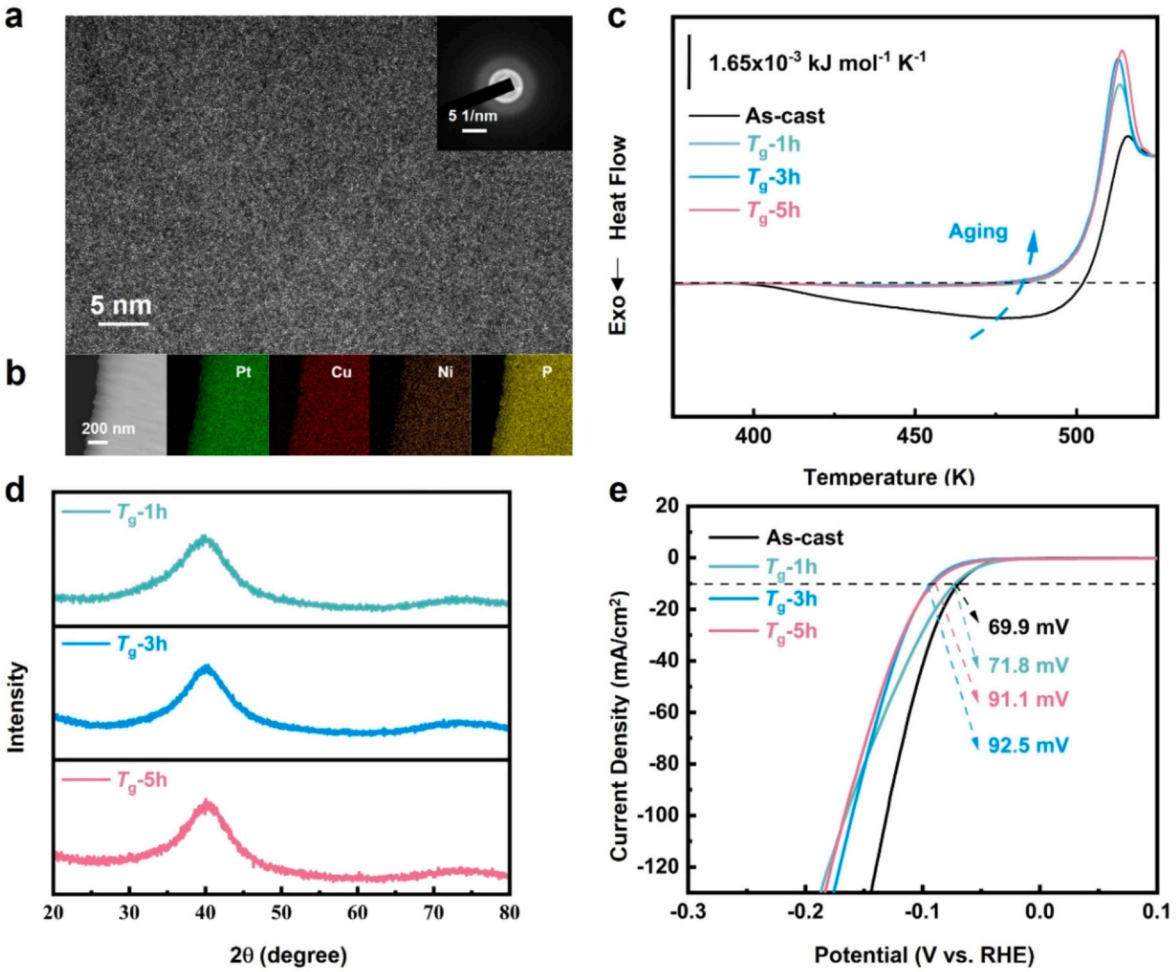

Fig. 1. Characterizations of the as-cast sample and aged samples. (a) The HRTEM image of as-cast sample. (b) The TEM elemental mapping results of as-cast sample. (c) The DSC curves of the as-cast and aged MGs. (d) The XRD patterns of aged MGs. (e) The HER polarization curves for as-cast sample and aged MGs acquired by LSV with a scan rate of 5 mV s^{-1} in 1 M KOH at room temperature.

the fully amorphous nature of the as-cast sample, which is consistent with the X-ray diffraction (XRD) results presented in Fig. S1 (Supporting Information). Transmission electron microscopy (TEM) imaging and complementary elemental mapping (Fig. 1b) reveal a uniform elemental distribution across the as-cast MGs.

A schematic of the annealing process is provided in Fig. S2a. To accelerate structural relaxation, samples were hermetically sealed, heated to the glass transition temperature (T_g), held for different

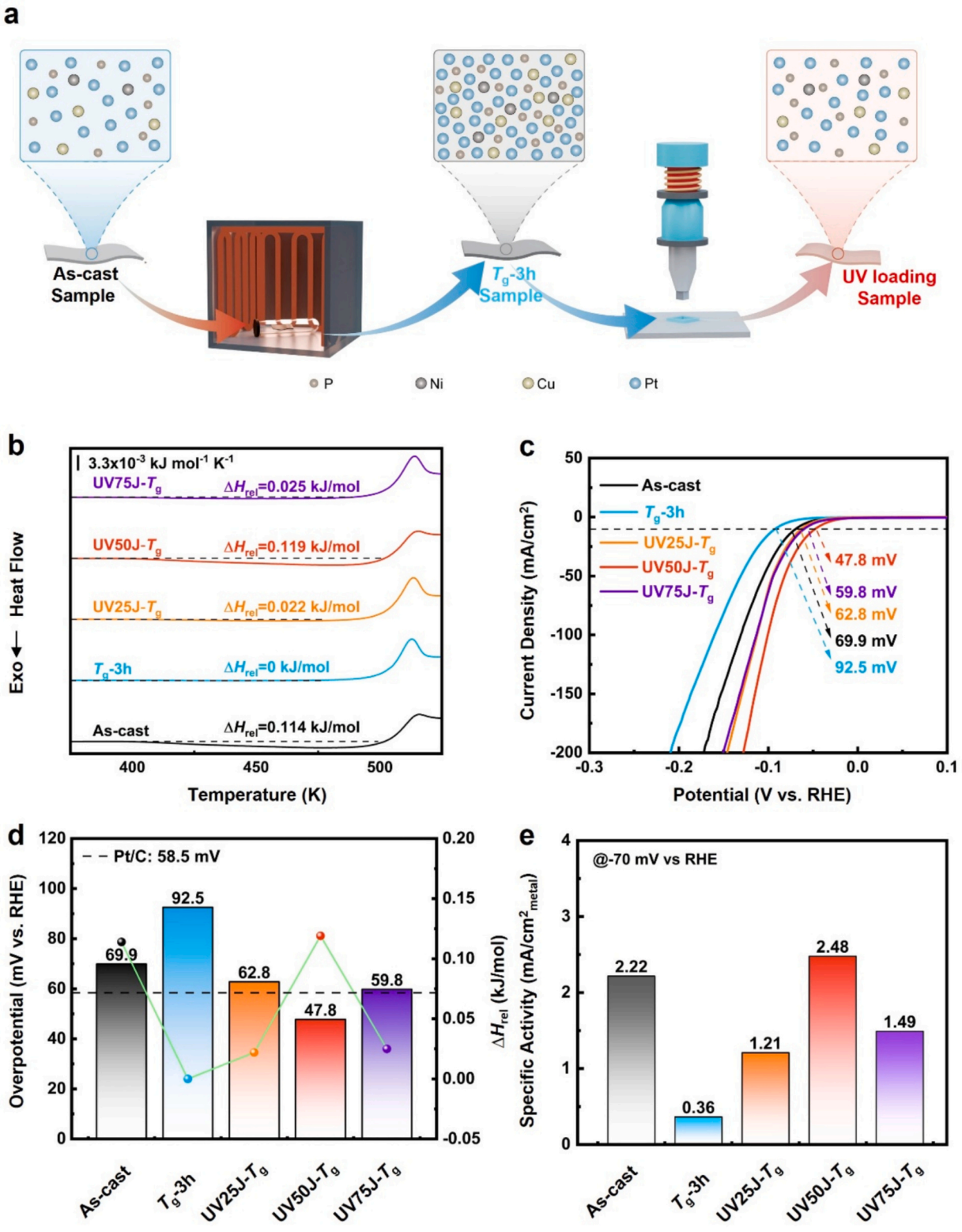

Fig. 2. The characterizations of UV loading samples. (a) The schematic diagram illustrates the UV loading process following the of the as-cast sample. (b) The DSC curves of the as-cast, T_g-3 h and UV loading samples. (c) The HER polarization curves for the as-cast, T_g-3 h and UV loading samples acquired by LSV with a scan rate of 5 mV s^{-1} in 1 M KOH at room temperature. (d) The overpotential and relaxation enthalpy evolution of the Pt/C, as-cast, T_g-3 h and UV loading samples. (e) The SA plots of the as-cast, T_g-3 h and UV loading samples at −70 mV (RHE).

durations (denoted as T_g-1 h, T_g-3 h, T_g-5 h), and then cooled to room temperature (Fig. S2b). Fig. 1c presents the differential scanning calorimetry (DSC) curves of the as-cast sample and its annealed derivatives. A broad exothermic peak below T_g is observed for the as-cast sample, indicating irreversible structural relaxation caused by the annihilation of excess free volume and other structural defects. [52–54] With increasing annealing time, this exothermic peak gradually diminishes, accompanied by a reduction in the structural relaxation enthalpy (ΔH_{rel}). When annealing exceeds 1 h, the sub-T_g exothermic signal disappears completely, and an overshoot above T_g emerges—consistent with previous reports. [54] XRD results confirm that all annealed samples remain amorphous (Fig. 1d).

Electrocatalytic properties of the annealed MGs were evaluated using a three-electrode configuration (previously reported [55,56]): a graphite rod as the counter electrode, Hg/HgO as the reference electrode, and the annealed MGs as the working electrode. Electrochemical tests were conducted in 1.0 M KOH at ambient temperature. Fig. 1e shows the linear sweep voltammetry (LSV) curves of the as-cast, T_g-1 h, T_g-3 h, and T_g-5 h samples, with current densities normalized to the electrode geometric area and corrected for 96% of total resistance. Potentials were converted to the reversible hydrogen electrode (RHE) scale using Eq. S1 (Supporting Information).

Significant variations in overpotentials at a current density of 10 mA cm^{-2} (η_{10}) were observed among the four samples. The η_{10} values s for T_g-1 h, T_g-3 h, and T_g-5 h samples are 71.8 mV, 90.1 mV, and 92.5 mV, respectively—all higher than the as-cast sample (69.9 mV). This trend aligns with the relaxation enthalpy: annealing at T_g reduces ΔH_{rel} relative to the pristine as-cast sample, corresponding to degraded catalytic performance. In summary, catalytic activity decreases progressively with extended annealing time.

Tafel plots were generated to analyze HER kinetics, with Tafel slopes calculated using Eq. S2 (Supporting Information). As shown in Fig. S3, the Tafel slope (plotted as overpotential η vs. log (−j)) is a key descriptor of HER kinetics—lower slopes indicate more favorable reaction pathways. [57] The Tafel slopes of the annealed samples are 51.28 mV dec^{-1} (T_g-1 h), 56.21 mV dec^{-1} (T_g-3 h), and 58.57 mV dec^{-1} (T_g-5 h), all higher than the as-cast sample (47.88 mV dec^{-1}). Notably, the Tafel's changes become more pronounced after longer annealing times (e.g., 3 h and 5 h). This further confirms that longer annealing time deteriorates catalytic performance.

2.2. Catalytic performance enhancement in MGs under UV loading

Previous studies have shown that ultrasonic loading can reverse the relaxation enthalpy in aged samples. [51] After 1 h of annealing, the ΔH_{rel} of the MGs essentially disappears; catalytic performance reaches its minimum after 3 h of annealing (η_{10} = 92.5 mV). Thus, the T_g-3 h sample was selected as the precursor for subsequent UV loading treatments.

Fig. 2a illustrates the schematic of the UV loading process. First, as-cast samples were annealed at T_g for 3 h to obtain aged T_g-3 h samples; subsequent UV loading yielded UV loading samples (denoted as UV25J-T_g, UV50J-T_g, UV75J-T_g). Atomic spacing of the aged sample is more compact than that of the as-cast sample; after UV loading treatment, atomic spacing re-expands to a more sparse configuration. These changes in atomic spacing are closely associated with variations in ΔH_{rel}, which will be discussed in detail below.

Fig. 2b presents the DSC curves of the as-cast, T_g-3 h, and UV-loaded samples. After prolonged annealing, ΔH_{rel} of the as-cast sample decreases from 0.114 kJ/mol to 0 kJ/mol. However, UV loading on the fully annealed sample restores ΔH_{rel}: with increasing UV energy, ΔH_{rel} of UV25J-T_g rises to 0.022 kJ/mol; UV50J-T_g exhibits a peak ΔH_{rel} of 0.119 kJ/mol (exceeding that of the as-cast sample); ΔH_{rel} of UV75J-T_g then decreases to 0.025 kJ/mol. XRD results confirm that all samples remain predominantly amorphous (Fig. S4). Notably, nanocrystals were observed in UV loading samples—it should be noted that the presence of a small amount of these nanocrystals slightly reduces the measured relaxation enthalpy value, implying that the theoretical ΔH_{rel} of the amorphous matrix after ultrasonic treatment might be higher. Nevertheless, the overall quantity of nanocrystals is limited, so their impact on the ΔH_{rel} measurement remains negligible. Their TEM characterization and influence on catalytic performance will be discussed in subsequent sections.

Fig. 2c shows the catalytic performance evolution of samples under different UV loading conditions. The black curve (as-cast reference) exhibits an η_{10} of 69.9 mV, while the T_g-3 h sample shows an increased η_{10} of 92.5 mV (significant performance degradation). In contrast, η_{10} of UV25J-T_g decreases to 62.8 mV; at 50 J UV energy, η_{10} of UV50J-T_g further reduces to 47.8 mV (lower than the as-cast sample). However, η_{10} of UV75J-T_g slightly increases to 59.88 mV. Thus, the UV50J-T_g sample exhibits the optimal catalytic performance.

Notably, the samples also perform excellently at high current densities (Fig. S5): the UV50J-T_g sample requires only 100.8 mV and 127.8 mV to achieve 100 mA cm^{-2} and 200 mA cm^{-2}, respectively. Tafel slope characterization (Fig. S6) further confirms this enhancement: the UV loading samples exhibit slopes of 37.23 mV dec^{-1} (UV50J-T_g), 42.27 mV dec^{-1} (UV25J-T_g), and 42.80 mV dec^{-1} (UV75J-T_g)—all much lower than the as-cast sample (47.88 mV dec^{-1}) and T_g-3 h sample (56.21 mV dec^{-1}). Lower Tafel slopes indicate more favorable HER kinetics, [57] confirming that UV loading on aged MGs significantly accelerates HER kinetics. HER in alkaline media proceeds via the Volmer step (water dissociation), followed by hydrogen recombination through either the Heyrovsky or Tafel step. The Tafel slopes of the as-cast, T_g-3 h, and UV loading samples are close to 40 mV dec^{-1}, indicating a Volmer–Heyrovsky mechanism with the Heyrovsky step as the rate-determining step. [58,59]

Electrochemical impedance spectroscopy (EIS) was conducted to elucidate charge transfer behavior (Fig. S7). A standard equivalent circuit (incorporating constant phase elements, series resistance Rs, and charge transfer resistance Rct [60]) was used to fit the EIS spectra. The UV50J-T_g sample exhibits a small Rs value; more importantly, the semicircle diameters of UV25J-T_g, UV50J-T_g, and UV75J-T_g are significantly reduced compared to the as-cast and T_g-3 h samples—indicating lower Rct. [61] Smaller semicircles reflect accelerated reaction rates and enhanced charge transfer efficiency, confirming that UV loading improves catalytic performance by promoting charge transfer.

Fig. 2d summarizes the evolution of η_{10} and ΔH_{rel} for the Pt/C, as-cast, T_g-3 h, and UV loading samples. During annealing, ΔH_{rel} decreases to 0 kJ/mol after 3 h, while η_{10} increases to 92.5 mV. After UV loading treatment, ΔH_{rel} first increases (peaking at 0.119 kJ/mol for UV50J-T_g) and then decreases with further UV energy input; η_{10} follows the inverse trend (minimum 47.8 mV at 50 J, which is lower than 58.5 MV of Pt/C catalyst). This strong correlation between ΔH_{rel} and η_{10} confirms that the intrinsic energy state of MGs significantly regulates their catalytic performance.

By comparing the electrochemical surface area (ECSA) normalized current density, we found that, at an overpotential of −70 mV (RHE), the specific activity (SA) values (calculated via Eqs. S3–S5, Fig. S8); follow the same trend as ΔH_{rel} (results in Fig. 2e and Fig. S9, Table S1). The UV50J-T_g sample exhibits the highest SA of 2.48 mA/cm^2_{metal}, representing an 11.7% increase compared to the as-cast sample (2.22 mA/cm^2_{metal}) and a 589% increase compared to the T_g-3 h sample (0.36 mA/cm^2_{metal}). These results confirm that UV loading effectively enhances the single-site catalytic activity of MGs.

Notably, annealing reduces the energy state and catalytic efficiency of as-cast MGs, while UV loading elevates the energy state of aged MGs (even exceeding the as-cast sample) and reduces η_{10} below the as-cast level. This indicates that UV loading enhances the activity of individual active sites by restoring the high-energy state of aged MGs, thereby improving overall catalytic performance.

In addition to its exceptional catalytic activity, the UV50J-T_g sample exhibits remarkable stability for the HER, as evidenced by the marginal

increase in potential over 84 h of continuous operation (Fig. S10). The LSV curve exhibits only a slight shift of 4 mV after 80 h, which is substantially lower than the 69.9 mV observed for the as-cast sample.

2.3. Reverse aging of fully aged MGs induced by UV loading

Ultrasonic vibration loading has been proven to rejuvenate amorphous materials, restoring their energy state to the initial level—a phenomenon widely recognized as "rejuvenation" or "reverse aging" in the field. [62] This study focuses on elucidating the mechanism underlying UV loading reverse aging. Fig. S11 shows ΔH_{rel} of aged MGs before and after UV loading treatment: the black curve corresponds to the as-cast sample; after 3 h of aging, ΔH_{rel} of the aged sample decreases to zero (blue curve); the red curve represents ΔH_{rel} of the aged sample after 50 J UV loading, which significantly increases (even slightly exceeding the as-cast sample).

Fig. 3a presents HRTEM images of the as-cast, T_g-3 h, and UV50J-T_g samples, along with the electron diffraction intensity of the halo ring in their SAED patterns. The halo ring radius increases with aging but decreases after UV loading. Average atomic spacing (Fig. 3b, c) is inversely proportional to the halo ring radius: the T_g-3 h sample exhibits smaller atomic spacing than the as-cast sample, indicating a denser amorphous structure. Notably, UV loading increases the atomic spacing of the aged sample, reverting its amorphous structure to a loosely packed state similar to the as-cast sample.

The energy state of MGs is positively correlated with their structural disorder—higher disorder corresponds to higher energy. [38] UV loading broadens the atomic spacing distribution of MGs, indicating increased structural disorder (in contrast to the ordering induced by relaxation [42]). Thus, from an atomic structural perspective, UV loading effectively reverses the aging of MGs.

The surface atomic activity of MGs significantly influences their catalytic performance, with higher energy states generally associated with enhanced atomic activity. Nanoindentation was used to analyze the modulus distribution of the three samples (a sensitive indicator of atomic activity [51]). Modulus maps (as-cast: Fig. 3d; T_g-3 h: Fig. 3e; UV50J-T_g: Fig. 3f) and statistical distributions (Fig. 3g) show the following modulus order: as-cast < UV50J-T_g < T_g-3 h. This trend is consistent with the average atomic spacing (Fig. 3c)—samples with larger atomic spacing exhibit lower modulus and hardness (Fig. 3h). Compared to the T_g-3 h sample, both the as-cast and UV50J-T_g samples show lower elastic modulus distributions (Fig. S12): the maximum elastic modulus values are 38 GPa (as-cast), 62 GPa (T_g-3 h), and 42 GPa (UV50J-T_g), respectively—consistent with previous reports that these two samples possess higher energy and enhanced surface atomic activity. [63] The indentation depths of the three samples under the same applied pressure follow the same trend (Fig. 3i), further confirming that UV loading elevates the energy state of aged MGs, achieving effective rejuvenation.

In MGs, high-energy states are typically accompanied by increased flow units (characterized by low atomic packing density and free volume). Free volume are defects characterized by a high-energy state, low density, and low modulus, as shown by the orange atom in Fig.S13a. [64,65] During annealing, free volume annihilation induces structural relaxation toward a lower energy state, resulting in densification and increased hardness/modulus (as shown by in Fig. 3h and the blue atom in Fig.S13b). However, UV loading introduces "negative flow units" (as shown by the green atom in Fig.S13c)—distinct from classical free volume-containing flow units—which exhibit higher atomic packing density and energy. [66] These negative flow units contain "anti-free volume," as confirmed by high-energy X-ray diffraction[41] and colloidal system experiments. [67] Thus, although the UV50J-T_g sample maintains a comparable or even higher energy state than the as-cast sample, the simultaneous introduction of free volume and anti-free volume via UV loading enables their mutual annihilation, ultimately leading to higher hardness and modulus than the as-cast sample.

2.4. Amorphous/crystalline (A/C) composite structures of UV loading improve catalytic performance

To investigate the intrinsic reason for the superior catalytic performance of UV loading samples compared to the as-cast sample, scanning electron microscopy (SEM) and TEM characterizations were conducted. SEM images (Fig. S14) show that the surface morphology of the T_g-3 h sample is similar to the as-cast sample; however, the UV50J-T_g sample exhibits a characteristic scaly wrinkle structure. This wrinkle formation is attributed to the as-cast preparation process: molten MGs is sprayed onto a rapidly rotating copper roller, undergoes rapid solidification, and forms bubble-like protrusions. During UV loading, high-frequency vibration compresses these protrusions into wrinkles. Elemental mapping (Fig. S15) confirms uniform elemental distribution in all three samples, with no signs of segregation or aggregation.

Fig. 4a–c present HRTEM images and corresponding Fourier transform patterns of the as-cast, T_g-3 h, and UV50J-T_g samples. The as-cast sample exhibits a typical amorphous structure (Fig. 4a), while the T_g-3 h sample contains a small number of fine nanocrystals (Fig. 4b). Notably, the UV50J-T_g sample shows significantly larger nanocrystals (Fig. 4c). To quantify nanocrystal size and distribution, TEM images were randomly selected from 9 regions (Figs. S16, S17) for statistical analysis (Fig. 4d). Compared to the annealed sample (fine, dispersed nanocrystals with an average size of 4.14 ± 2.60 nm), the UV loading sample exhibits larger (5.4 ± 2.71 nm), denser, and more abundant nanocrystals—indicating that UV loading promotes nanocrystal growth and proliferation in aged MGs.

In addition, we performed quantitative analyses of crystallinity and interface density for the T_g-3 h and UV50J-T_g samples, as shown in Fig. S18a-b. The crystallinity of UV50J-T_g is 15%, which is significantly higher than the 4% observed for T_g-3 h. This result is consistent with the trend observed in the statistical analysis of nanocrystal size. Based on 9 randomly selected TEM regions for each sample (consistent with the areas shown in Figs. S16 and S17), we statistically determine the area fraction occupied by the crystalline phase (Fig. S18c-d). The results are 4% for T_g-3 h and 15% for UV50J-T_g, which are in agreement with the XRD refinement data. Meanwhile, we have also performed a quantitative calculation of the phase interface density based on the same set of TEM images. This increase in interface density after UV loading (from 0.033 nm/nm^2 to 0.102 nm/nm^2) provides direct evidence that the formation of the A/C composite structure, particularly the generation of abundant phase interfaces. Energy dispersive spectroscopy (EDS) spectrum (Fig. 4e) confirms uniform elemental distribution in UV50J-T_g, with no segregation or aggregation. These results demonstrate that UV loading effectively introduces crystalline phases into the amorphous matrix, forming an A/C composite structure.

A/C composite structures integrate the high electrical conductivity of crystalline phases and the abundant unsaturated coordination sites of amorphous phases—an architecture proven to significantly enhance catalytic performance. [68–72] Two key synergistic effects contribute to this enhancement: (1) Potential mismatch between crystalline grains and the amorphous matrix generates free electrons, accelerating reaction rates; [72–74] (2) Abundant phase boundaries and high kinetic energy of A/C composites provide more accessible active sites and facilitate mass diffusion/charge transfer. [68,75–77]

Combined with the foregoing analysis of ECSA-normalized current densities (Fig. S9d), we can now rationalize why the fully aged and relaxed sample exhibits markedly improved catalytic performance after UV loading—even surpassing that of the pristine as-cast specimen. UV loading not only restores the aged sample to its pre-aging high-energy state but also enhances the intrinsic activity of active sites through the introduction of A/C composite structures. This synergistic effect elevates the catalytic performance beyond that of the initial as-cast sample, which possesses only a single-phase amorphous structure. To further elucidate this mechanism, we conducted theoretical calculations.

The Gibbs free energy of hydrogen adsorption (ΔG_{H^*}) is a pivotal

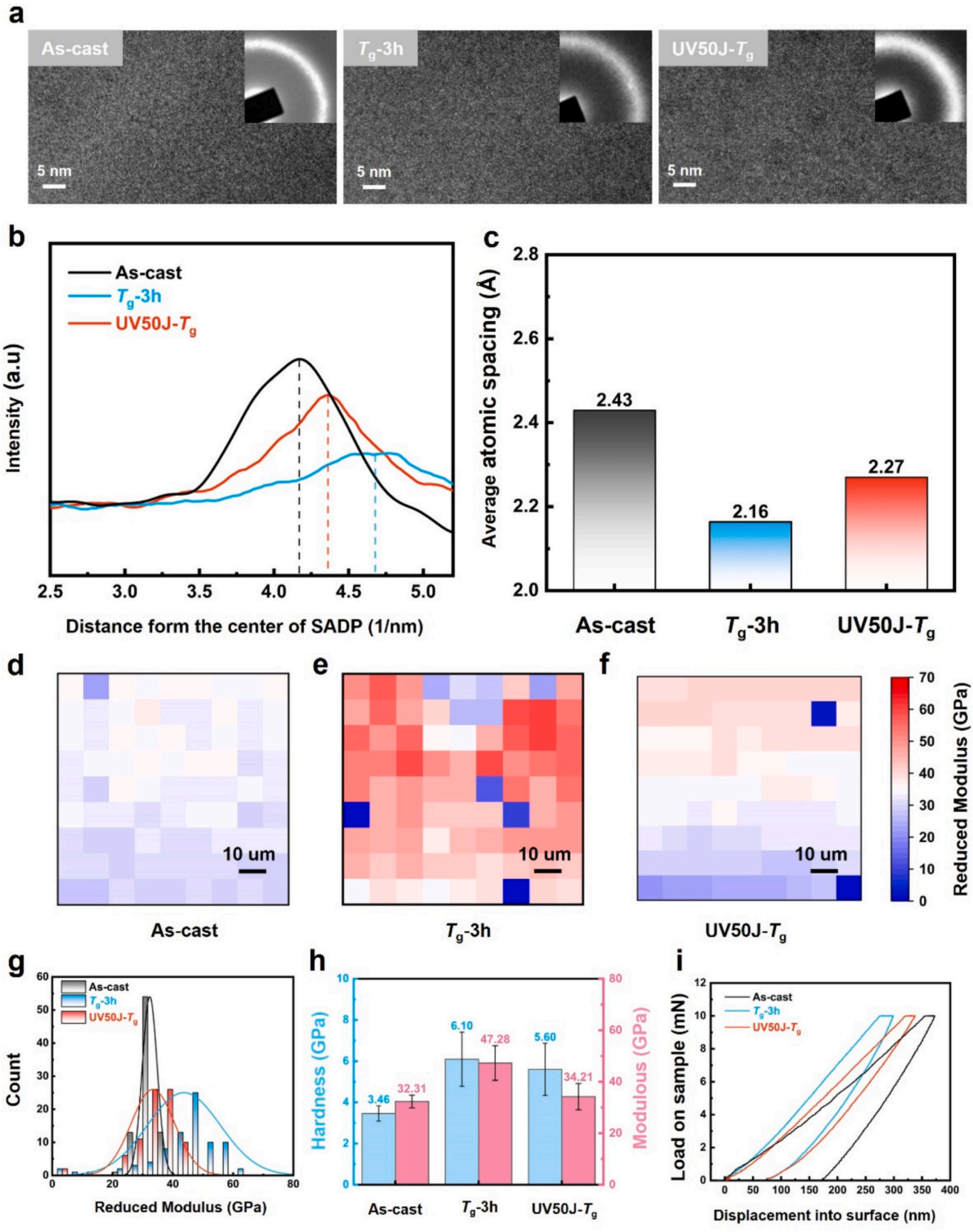

Fig. 3. (a) The HRTEM images of the three samples and the electron diffraction intensity of the halo ring in the SAED pattern are shown: the as-cast, the T_g-3 h, and the UV50J-T_g. (b) Diffraction ring radius obtained by SAED in (a). (c) Average atomic spacing obtained by diffraction ring radius. (d-f) The dynamic modulus mapping of the as-cast, the T_g-3 h, and the UV50J-T_g. (g) Modulus distribution histogram of the as-cast, the T_g-3 h, and the UV50J-T_g. (h) Comparison of the hardness and modulus between the as-cast, the T_g-3 h, and the UV50J-T_g. (i) Load-displacement curve for the as-cast, the T_g-3 h and the UV50J-T_g.

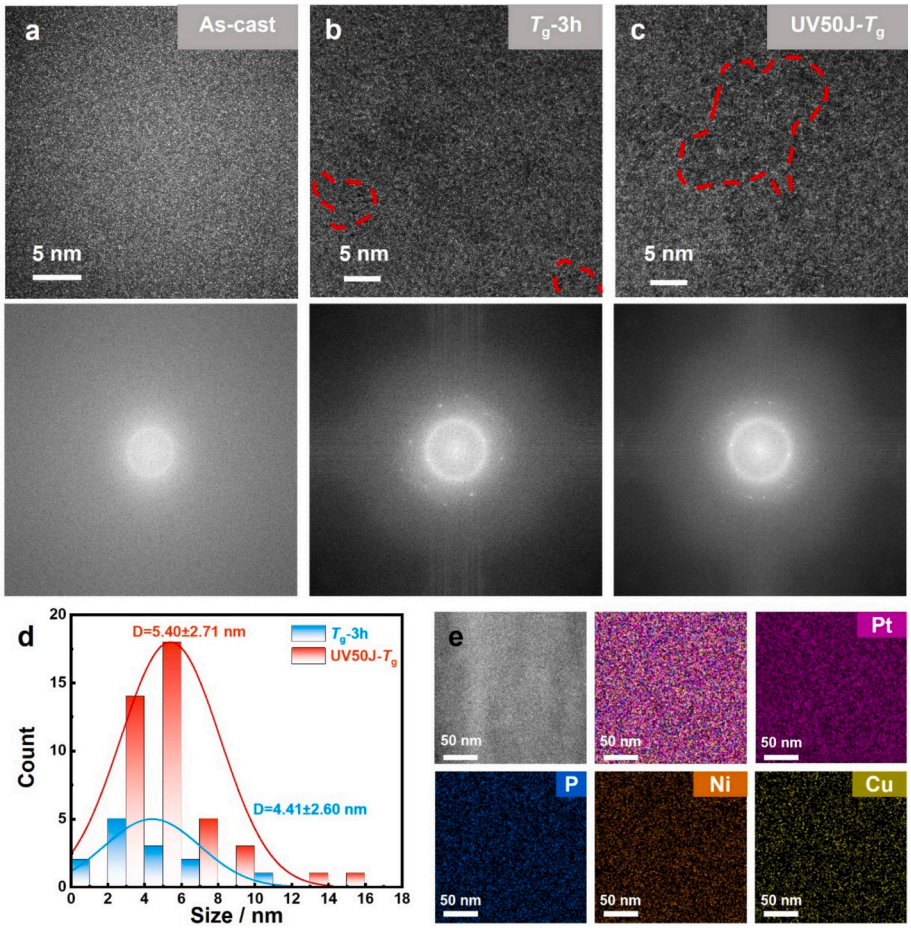

Fig. 4. The HRTEM images of the as-cast (a), T_g-3 h (b), and UV50J-T_g (c), along with their corresponding Fourier transform images. (d) The distribution and size of the nanocrystals of T_g-3 h sample and UV50J-T_g sample. (e) The EDS of UV50J-T_g sample.

descriptor for HER activity—values approaching the thermoneutral point (ΔGH = 0 eV) indicate optimal adsorption-desorption kinetics. [78] To elucidate the effect of A/C composite structures on hydrogen adsorption energetics, first-principles density functional theory (DFT) calculations were performed to compare partially crystalline MGs (A/C-MG) and fully amorphous MGs.

As shown in Fig. S19a, the calculated ΔG_h* values differ significantly between the two systems: 0.30 eV for A/C-MG versus 0.59 eV for fully amorphous MGs. This 0.29 eV reduction brings hydrogen binding closer to the optimal thermodynamic range, confirming that A/C structures optimize hydrogen binding through crystalline-amorphous synergy. This balanced adsorption-desorption lowers the activation barrier for rate-determining steps, enhancing catalytic kinetics.

The optimized H* adsorption on A/C-MG (Fig. S19b) shows a distinct charge density distribution that facilitates hydrogen interactions. Differential charge analysis reveals electron transfer from H* to adjacent Pt atoms, weakening H—H bonds and reducing the desorption barrier. A/C-MG's superior performance stems from its hybrid architecture (Fig. S19c, d): nanocrystalline regions provide high conductivity and defined active sites, while the amorphous matrix offers unsaturated coordination sites. This creates a dual-function surface—crystalline areas enable fast charge transfer, and amorphous areas increase active site density through structural disorder. DFT confirms that partial crystallization tunes both electronic structure and hydrogen adsorption energy, driving the enhanced HER activity observed experimentally.

To differentiate the contributions of recovered energy state versus introduced A/C composite structure, we prepared a control sample (0.8T_g-3 h) by thermally treating the as-cast sample at 0.8T_g for 3 h without UV loading. This 0.8T_g-3 h exhibits an intermediate energy state between the fully amorphous as-cast and fully relaxed Tg-3 h samples (Fig. S20a), with a comparable crystalline fraction of ~3% (Fig. S20b). The higher-energy-state 0.8T_g-3 h sample shows lower overpotential than T_g-3 h (4%) at similar crystalline fraction (Fig. S20c). This further corroborates our conclusion that the energy state significantly influences catalytic performance—higher relaxation enthalpy corresponds to higher energy state and better catalytic activity. Notably, UV50J-T_g possesses a higher energy state than both T_g-3 h and 0.8T_g-3 h, with correspondingly superior catalytic performance, confirming that energy state recovery via UV loading contributes to the enhanced catalytic activity.

Furthermore, comparison between as-cast and UV50J-T_g at equivalent energy states (Fig. S20a and c) reveals that UV50J-T_g (crystalline fraction: 14%) exhibits lower overpotential than the single-phase amorphous as-cast sample (0%). This directly validates that A/C composite structure introduction additionally enhances catalytic performance.

In summary, UV loading treatment enhances catalytic performance through the synergistic contribution of two factors: (i) reversal of aging and recovery of high energy state, and (ii) introduction of A/C composite structure. This synergistic mechanism transforms the fully aged/relaxed low-energy-state sample into a high-performance catalyst.

2.5. *The application of UV loading strategy for Pd-MGs*

To verify the general applicability of the UV loading strategy, Pd-based MGs (Pd-MG) were further investigated. The energy state

evolution of Pd-MG is consistent with Pt-MG: aging reduces the energy state, while UV loading restores it (Fig. S21a). Specifically, after annealing, the ΔH_{rel} of Pd-MG decreases from 0.531 kJ/mol to 0.158 kJ/mol (Pd-MG-T_g); UV loading recovers ΔH_{rel} to 0.319 kJ/mol (Pd-MG-T_g-UV).

Under identical experimental conditions, the HER activity trend of Pd-MG mirrors its energy state evolution (Fig. S21b). After annealing, η_{10} of Pd-MG increases from 87 mV to 106.9 mV (Pd-MG-T_g); UV loading reduces η_{10} to 67.0 mV (Pd-MG-T_g-UV)—representing a 39.9 mV reduction compared to Pd-MG-T_g and a 20.7 mV reduction compared to pristine Pd-MG. Tafel slope characterization (Fig. S21c) confirms this enhancement: the slope increases from 90.55 mV dec^{-1} (Pd-MG) to 98.62 mV dec^{-1} (Pd-MG-T_g) after annealing, and decreases to 78.65 mV dec^{-1} after UV loading (Pd-MG-T_g-UV).

At an overpotential of −70 mV (RHE), the SA value of Pd-MG samples (Fig. S21d, calculated via Figs. S22, S23) follows the same trend as η_{10} (Fig. S21b). The Pd-MG-T_g-UV sample exhibits the highest SA of 1.04 mA/cm$^2_{metal}$—1.31 times higher than pristine Pd-MG (0.45 mA/cm$^2_{metal}$) and 2.25 times higher than Pd-MG-T_g (0.32 mA//cm$^2_{metal}$). This confirms that the UV loading strategy effectively enhances the single-site catalytic activity of Pd-MG.

In conclusion, the UV loading strategy exhibits broad applicability, being effective for both Pt-based and Pd-based MGs.

2.6. *Investigating the effect of UV loading on the catalytic properties of MGs*

Figs. 3 and 4 illustrate the reverse aging process and the associated enhancement in catalytic performance achieved through the UV loading strategy. These intriguing phenomena are analyzed and interpreted within the framework of the potential energy landscape (PEL) theory, as shown in Fig. 5. The PEL illustrates the potential energy minima/metabasins associated with various configurations. The deepest energy minima correspond to stabilized crystalline phases, while the shallower minima represent metastable glassy states. [79]

As-cast MGs are formed through the rapid cooling of the melt, during which deep and narrow potential energy pits are easily bypassed due to the fast cooling rate, trapping the material in a relatively high-energy metastable state (black dot in Fig. 5). During the annealing process at T_g, atomic mobility increases, allowing the as-cast MGs to transition toward a more thermodynamically stable state by moving to lower-energy basins in the PEL. With sufficient aging time (3 h in this study), the energy state of the aged MGs reaches a relatively low level (blue dot labeled "Fully Aged" in Fig. 5), resulting in the disappearance of the exothermic peak in the DSC curve (blue curve for T_g-3 h sample). The reduction in energy is accompanied by an increase in surface modulus (Fig. 3h), suggesting a decrease in surface atomic activity. This reduction in surface atomic activity leads to a decline in the catalytic activity of individual active sites and an increase in overpotential, ultimately resulting in diminished overall catalytic performance.

Interestingly, application of UV loading can excite the system from the low-energy state after aging to a higher energy state by imparting mechanical energy, driving atomic rearrangement and jumping to higher-energy metastable basins (red dot labeled "Reverse Aging" in Fig. 5). This energy elevation reduces the hardness and modulus to levels comparable to those of the as-cast sample (Fig. 3h) and induces the reappearance of the exothermic peak (red curve for UV50J-T_g sample in Fig. 5). These changes enhance the catalytic activity of samples.

Notably, compared with the as-cast sample possessing a single amorphous structure, the UV loading sample (UV50J-T_g) exhibits a higher proportion of A/C composite structure (see Figs. 4 and S18). Concurrently, its specific activity (SA) is 11.7% higher than that of the as-cast sample, with a lower overpotential as well (see Figs. 2d and e). This finding effectively precludes the possibility that the catalytic

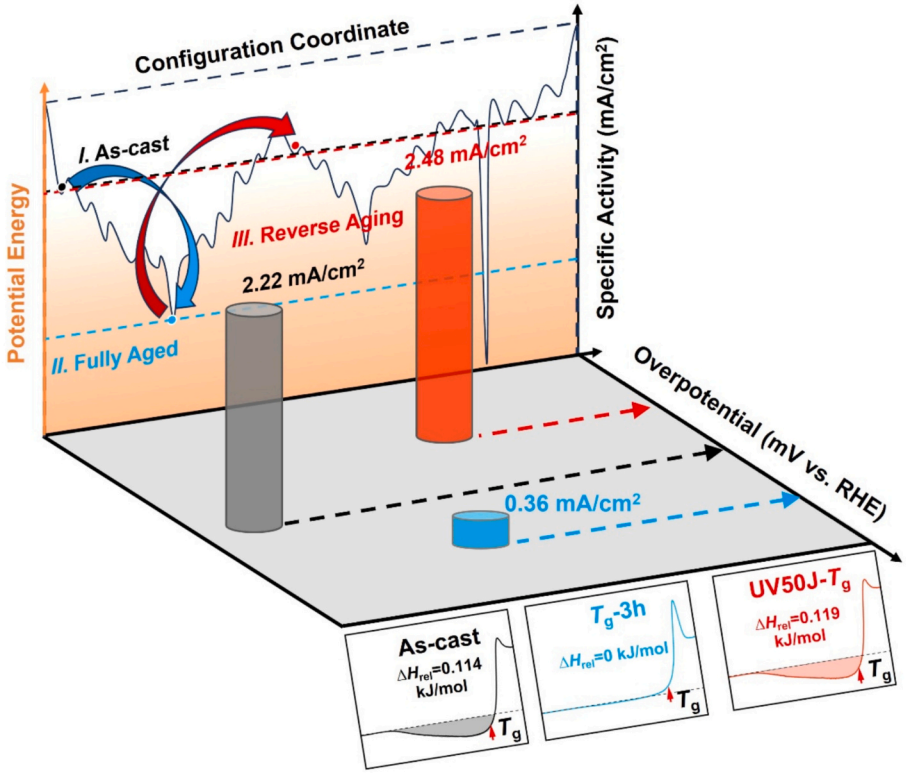

Fig. 5. Explain the annealing process of MGs and UV loading -induced reverse aging, as well as the relationship with catalytic performance. The diagram of the leftmost orange background is Schematic diagram of the potential energy landscape of MGs. The change in the energy state of MGs during aging (blue arrows). The change in the energy state of aged MGs during UV loading (red arrow). The histogram in the middle is the SA value of the as-cast sample, T_g-3 h sample and UV50J-T_g sample, and the corresponding overpotential change. The three illustrations below are the DSC curves of MGs.

enhancement of UV50J-T_g arises solely from aging reversal and energy state recovery. Rather, it provides direct evidence that UV irradiation not only restores the fully relaxed sample to its pre-aging energetic state, but also introduces A/C composite structure. Through the synergistic effect of the high conductivity of the crystalline phase and the abundant active sites in the amorphous phase, the intrinsic activity of active sites is further enhanced, thereby achieving superior catalytic performance compared to the pristine as-cast sample.

To further highlight the superiority of the UV loading samples, the η_{10} and Tafel slope of UV50J-T_g for HER were compared with those of various electrocatalysts documented in the literature, including Pt-based, Ag-based, Pd-based, Rh-based, and Ir-based metals. The detailed comparison is presented in Fig. S24 and Table S2. It was found that UV50J-T_g exhibits lower overpotentials for HER in alkaline media and demonstrates exceptional catalytic performance among the compared materials. This underscores the great potential of UV loading MGs as high-performance catalysts in electrolytic systems.

3. Conclusions

This work develops an UV loading strategy to address catalytic degradation of fully aged MGs. UV loading reverses structural relaxation, restoring MGs' high-energy state (ΔH_{rel} up to 0.119 kJ/mol) and inducing nanocrystal formation, constructing amorphous/crystalline dual-phase structures. These effects synergistically boost HER performance, with UV50J-T_g showing η_{10} of 47.8 mV (lower than aged and as-cast MGs). Notably, this strategy works for both Pt- and Pd-MGs, offering a versatile tool to regulate MGs surface energy and paving new ways for designing high-performance amorphous catalysts.

CRediT authorship contribution statement

Shenghao Zeng: Writing – original draft, Visualization, Methodology, Investigation, Data curation, Conceptualization. **Wenqing Ruan:** Writing – review & editing, Supervision, Data curation, Conceptualization. **Jianyu Chen:** Methodology, Data curation. **Zhe Chen:** Investigation. **Jihan Jiang:** Investigation, Conceptualization. **Xiaodi Liu:** Supervision, Methodology. **Qing Chen:** Methodology, Data curation. **Shuai Ren:** Supervision, Resources, Methodology. **Xiong Liang:** Supervision, Resources. **Jiang Ma:** Writing – review & editing, Visualization, Supervision, Resources, Conceptualization.

Declaration of competing interest

The authors declare that they have no known competing financial interests or personal relationships that could have appeared to influence the work reported in this paper.

Acknowledgments

The work was financially supported by the Key-Area Research and Development Program of Guangdong Province (Grant No. 2024B0101070001), the NSF of China (Grant Nos. 52401217, 52571191, 52271150, 52571190), Advanced Materials-National Science and Technology Major Project (Grant No. 2025ZD0619204), the Science, Technology and Innovation Commission of Shenzhen Municipality (Grants No. RCJC20221008092730037, JCYJ202506 04182240052, JCYJ20240813141413018), the Research Team Cultivation Program of Shenzhen University (Grant No. 2023QNT001). We thank the Instrumental Analysis Center of Shenzhen University for the assistance with the Electron Microscope. The computational work was carried out on the public computing service platform provided by the Network and Computing Center of HUST.

Appendix A. Supplementary data

Supplementary data to this article can be found online at https://doi.org/10.1016/j.cej.2026.175881.

Data availability

Data will be made available on request.

References

[1] H.B. Yu, M. Tylinski, A. Guiseppi-Elie, M.D. Ediger, R. Richert, Suppression of β relaxation in vapor-deposited Ultrastable glasses, Phys. Rev. Lett. 115 (18) (2015) 185501, https://doi.org/10.1103/PhysRevLett.115.185501.
[2] J. Ma, C. Yang, X. Liu, B. Shang, Q. He, F. Li, T. Wang, D. Wei, X. Liang, X. Wu, Y. Wang, F. Gong, P. Guan, W. Wang, Y. Yang, Fast surface dynamics enabled cold joining of metallic glasses, Sci. Adv. 5 (11) (2019) eaax7256, https://doi.org/10.1126/sciadv.aax7256.
[3] H. Wagner, D. Bedorf, S. Küchemann, M. Schwabe, B. Zhang, W. Arnold, K. Samwer, Local elastic properties of a metallic glass, Nat. Mater. 10 (6) (2011) 439–442, https://doi.org/10.1038/nmat3024.
[4] S. Baranov, V. Larin, A. Torcunov, Technology, preparation and properties of the cast glass-coated magnetic microwires, Crystals 7 (6) (2017) 136, https://doi.org/10.3390/cryst7060136.
[5] Y. Liu, X. Liu, A.R. Jadhav, T. Yang, Y. Hwang, H. Wang, L. Wang, Y. Luo, A. Kumar, J. Lee, H.T.D. Bui, M. Gyu Kim, H. Lee, Unraveling the function of metal–amorphous support interactions in single-atom electrocatalytic hydrogen evolution, Angew. Chem. 134 (9) (2022), https://doi.org/10.1002/ange.202114160.
[6] J. Masa, P. Weide, D. Peeters, I. Sinev, W. Xia, Z. Sun, C. Somsen, M. Muhler, W. Schuhmann, Amorphous cobalt boride (Co_2B) as a highly efficient nonprecious catalyst for electrochemical water splitting: oxygen and hydrogen evolution, Adv. Energy Mater. 6 (6) (2016) 1502313, https://doi.org/10.1002/aenm.201502313.
[7] J.S. Kim, I. Park, E.S. Jeong, K. Jin, W.M. Seong, G. Yoon, H. Kim, B. Kim, K. T. Nam, K. Kang, Amorphous cobalt phyllosilicate with layered crystalline motifs as water oxidation catalyst, Adv. Mater. 29 (21) (2017) 1606893, https://doi.org/10.1002/adma.201606893.
[8] G. Chen, Y. Zhu, H.M. Chen, Z. Hu, S.F. Hung, N. Ma, J. Dai, H.J. Lin, C.T. Chen, W. Zhou, Z. Shao, An amorphous nickel–Iron-based Electrocatalyst with unusual local structures for ultrafast oxygen evolution reaction, Adv. Mater. 31 (28) (2019) 1900883, https://doi.org/10.1002/adma.201900883.
[9] Y.C. Hu, Y.Z. Wang, R. Su, C.R. Cao, F. Li, C.W. Sun, Y. Yang, P.F. Guan, D.W. Ding, Z.L. Wang, A highly efficient and self-stabilizing metallic-glass catalyst for electrochemical hydrogen generation, Adv. Mater. 28 (46) (2016) 10293–10297, https://doi.org/10.1002/adma.201603880.
[10] F. Hu, S. Zhu, S. Chen, Y. Li, L. Ma, T. Wu, Y. Zhang, C. Wang, C. Liu, X. Yang, L. Song, X. Yang, Y. Xiong, Amorphous metallic NiFeP: a conductive bulk material achieving high activity for oxygen evolution reaction in both alkaline and acidic media, Adv. Mater. 29 (32) (2017) 1606570, https://doi.org/10.1002/adma.201606570.
[11] Y. Yan, C. Wang, Z. Huang, J. Fu, Z. Lin, X. Zhang, J. Ma, J. Shen, Highly efficient and robust catalysts for the hydrogen evolution reaction by surface nano engineering of metallic glass, J. Mater. Chem. A 9 (9) (2021) 5415–5424, https://doi.org/10.1039/d0ta10235k.
[12] Z. Jia, K. Nomoto, Q. Wang, C. Kong, L. Sun, L.C. Zhang, S.X. Liang, J. Lu, J. J. Kruzic, A self-supported high-entropy metallic glass with a Nanosponge architecture for efficient hydrogen evolution under alkaline and acidic conditions, Adv. Funct. Mater. 31 (38) (2021) 2101586, https://doi.org/10.1002/adfm.202101586.
[13] J. Qin, H. Zhang, W. Lu, J. Zhu, J. Tian, J. Shen, Nanoporous NiPt alloy by dealloying of amorphous NiZrPt metallic glass for alkaline hydrogen evolution reaction, Chem. Eng. J. 490 (2024) 151700, https://doi.org/10.1016/j.cej.2024.151700.
[14] J. Jiang, W. Ruan, S. Zeng, J. Lin, X. Zhao, J. Fu, Q. Chen, X. Liu, J. Ma, Self-supported partially crystallized nanoporous metallic glass for ultra-stable and efficient electrocatalytic hydrogen evolution, Sci. China-Mater. (2026) 1–12, https://doi.org/10.1007/s40843-025-3506-3.
[15] X. Guo, W. Zhang, R. Shi, H. Zhu, C. Qian, H. Yang, J. Zhang, A. Yuan, Y. Zhou, Facile fabrication of amorphous Ni−P supported on a 3D biocarbon skeleton as an efficient Electrocatalyst for the oxygen evolution reaction, ChemElectroChem 6 (12) (2019) 3071–3076, https://doi.org/10.1002/celc.201900458.
[16] Y. Jin, G. Xi, R. Li, Z.-A. Li, X.-B. Chen, T. Zhang, Nanoporous metallic-glass electrocatalysts for highly efficient oxygen evolution reaction, J. Alloys Compd. 852 (2021) 156876, https://doi.org/10.1016/j.jallcom.2020.156876.
[17] B. Sarac, Y.P. Ivanov, M. Micusik, M. Omastova, A.S. Sarac, A.I. Bazlov, V. Zadorozhnyy, A.L. Greer, J. Eckert, Enhanced oxygen evolution reaction of Zr-cu-Ni-Al metallic glass with an oxide layer in alkaline media, ACS Catal. 12 (15) (2022) 9190–9200, https://doi.org/10.1021/acscatal.2c02672.
[18] A. Simonov, A.L. Goodwin, Designing disorder into crystalline materials, Nat. Rev. Chem. 4 (12) (2020) 657–673, https://doi.org/10.1038/s41570-020-00228-3.
[19] G. Prieto, S. Beijer, M.L. Smith, M. He, Y. Au, Z. Wang, D.A. Bruce, K.P. De Jong, J. J. Spivey, P.E. De Jongh, Design and synthesis of copper–cobalt catalysts for the

selective conversion of synthesis gas to ethanol and higher alcohols, Angew. Chem. 126 (25) (2014) 6515–6519, https://doi.org/10.1002/ange.201402680.
[20] W. Huang, W.-X. Li, Surface and interface design for heterogeneous catalysis, Phys. Chem. Chem. Phys. 21 (2) (2019) 523–536, https://doi.org/10.1039/c8cp05717f.
[21] S.L. Bernasek, G.A. Somorjai, Small molecule reactions on stepped single crystal platinum surfaces, Surf. Sci. 48 (1) (1975) 204–213, https://doi.org/10.1016/0039-6028(75)90317-9.
[22] N. Lebedeva, A. Rodes, J. Feliu, M. Koper, R. Van Santen, Role of crystalline defects in electrocatalysis: CO adsorption and oxidation on stepped platinum electrodes as studied by in situ infrared spectroscopy, J. Phys. Chem. B 106 (38) (2002) 9863–9872, https://doi.org/10.1021/jp0203806.
[23] T. Sheng, Y.-F. Xu, Y.-X. Jiang, L. Huang, N. Tian, Z.-Y. Zhou, I. Broadwell, S.-G. Sun, Structure design and performance tuning of nanomaterials for electrochemical energy conversion and storage, Acc. Chem. Res. 49 (11) (2016) 2569–2577, https://doi.org/10.1021/acs.accounts.6b00485.
[24] H. Zhang, M. Jin, Y. Xiong, B. Lim, Y. Xia, Shape-controlled synthesis of Pd nanocrystals and their catalytic applications, Acc. Chem. Res. 46 (8) (2013) 1783–1794, https://doi.org/10.1021/ar300209w.
[25] N.S. Porter, H. Wu, Z. Quan, J. Fang, Shape-control and electrocatalytic activity-enhancement of Pt-based bimetallic nanocrystals, Acc. Chem. Res. 46 (8) (2013) 1867–1877, https://doi.org/10.1021/ar3002238.
[26] Q. Chen, Y. Jia, S. Xie, Z. Xie, Well-faceted noble-metal nanocrystals with nonconvex polyhedral shapes, Chem. Soc. Rev. 45 (11) (2016) 3207–3220, https://doi.org/10.1039/c6cs00039h.
[27] J. Wang, L. Han, B. Huang, Q. Shao, H.L. Xin, X. Huang, Amorphization activated ruthenium-tellurium nanorods for efficient water splitting, Nat. Commun. 10 (1) (2019) 5692, https://doi.org/10.1038/s41467-019-13519-1.
[28] X. Zhang, Z. Luo, P. Yu, Y. Cai, Y. Du, D. Wu, S. Gao, C. Tan, Z. Li, M. Ren, T. Osipowicz, S. Chen, Z. Jiang, J. Li, Y. Huang, J. Yang, Y. Chen, C.Y. Ang, Y. Zhao, P. Wang, L. Song, X. Wu, Z. Liu, A. Borgna, H. Zhang, Lithiation-induced amorphization of Pd3P2S8 for highly efficient hydrogen evolution, Nat. Catal. 1 (6) (2018) 460–468, https://doi.org/10.1038/s41929-018-0072-y.
[29] J. Wang, L. Han, B. Huang, Q. Shao, H.L. Xin, X. Huang, Amorphization activated ruthenium-tellurium nanorods for efficient water splitting, Nat. Commun. 10 (1) (2019) 5692, https://doi.org/10.1038/s41467-019-13519-1.
[30] G. Chen, Y. Zhu, H.M. Chen, Z. Hu, S.F. Hung, N. Ma, J. Dai, H.J. Lin, C.T. Chen, W. Zhou, An amorphous nickel–iron-based electrocatalyst with unusual local structures for ultrafast oxygen evolution reaction, Adv. Mater. 31 (28) (2019) 1900883, https://doi.org/10.1002/adma.201900883Digital.
[31] L.C.E. Struik, Physical aging in amorphous polymers and other materials, in: No Title, 1978.
[32] J. Chen, S. Ren, Z. Chen, J. Dong, L. Zhu, Y. Zhan, W. Wang, S. Zeng, J. Xiao, X. Liang, Unveiling irreversible β-relaxations in metallic glasses via electrical resistivity, Metals 15 (2) (2025) 196, https://doi.org/10.3390/met15020196.
[33] I.M. Hodge, Physical aging in polymer glasses, Science 267 (5206) (1995) 1945–1947, https://doi.org/10.1126/science.267.5206.1945.
[34] R. Casalini, C. Roland, Aging of the secondary relaxation to probe structural relaxation in the glassy state, Phys. Rev. Lett. 102 (3) (2009) 035701, https://doi.org/10.1103/PhysRevLett.102.035701.
[35] Y. Sun, A. Concustell, A.L. Greer, Thermomechanical processing of metallic glasses: extending the range of the glassy state, Nature Reviews Materials 1 (9) (2016) 16039, https://doi.org/10.1038/natrevmats.2016.39.
[36] P. Ross, S. Küchemann, P.M. Derlet, H. Yu, W. Arnold, P. Liaw, K. Samwer, R. Maaß, Linking macroscopic rejuvenation to nano-elastic fluctuations in a metallic glass, Acta Mater. 138 (2017) 111–118, https://doi.org/10.1016/j.actamat.2017.07.043.
[37] S.-C. Lee, C.-M. Lee, J.-W. Yang, J.-C. Lee, Microstructural evolution of an elastostatically compressed amorphous alloy and its influence on the mechanical properties, Scr. Mater. 58 (7) (2008) 591–594, https://doi.org/10.1016/j.scriptamat.2007.11.036.
[38] Y. Sun, A. Concustell, A.L. Greer, Thermomechanical processing of metallic glasses: extending the range of the glassy state, Nat. Rev. Mater. 1 (9) (2016) 1–14, https://doi.org/10.1038/natrevmats.2016.39.
[39] S.V. Ketov, Y.H. Sun, S. Nachum, Z. Lu, A. Checchi, A.R. Beraldin, H.Y. Bai, W. H. Wang, D.V. Louzguine-Luzgin, M.A. Carpenter, A.L. Greer, Rejuvenation of metallic glasses by non-affine thermal strain, Nature 524 (7564) (2015) 200–203, https://doi.org/10.1038/nature14674.
[40] T. Lei, L.R. DaCosta, M. Liu, W. Wang, Y. Sun, A. Greer, M. Atzmon, Microscopic characterization of structural relaxation and cryogenic rejuvenation in metallic glasses, Acta Mater. 164 (2019) 165–170, https://doi.org/10.1016/j.actamat.2018.10.036.
[41] K. Sun, G. Wang, Y. Wang, H. Chen, L. Yan, S. Pauly, Y. Wu, H. Weber, Q. Wang, B. Huang, Structural rejuvenation and relaxation of a metallic glass induced by ion irradiation, Scr. Mater. 180 (2020) 34–39, https://doi.org/10.1016/j.scriptamat.2020.01.023.
[42] W. Dmowski, Y. Yokoyama, A. Chuang, Y. Ren, M. Umemoto, K. Tsuchiya, A. Inoue, T. Egami, Structural rejuvenation in a bulk metallic glass induced by severe plastic deformation, Acta Mater. 58 (2) (2010) 429–438, https://doi.org/10.1016/j.actamat.2009.09.021.
[43] J. Dong, Y.-H. Feng, Y. Huan, J. Yi, W.-H. Wang, H.-Y. Bai, B.-A. Sun, Rejuvenation in hot-drawn micrometer metallic glassy wires*, Chin. Phys. Lett. 37 (1) (2020) 017103, https://doi.org/10.1088/0256-307x/37/1/017103.
[44] R.M.O. Mota, E.T. Lund, S. Sohn, D.J. Browne, D.C. Hofmann, S. Curtarolo, A. Van De Walle, J. Schroers, Enhancing ductility in bulk metallic glasses by straining during cooling, Commun. Mater. 2 (1) (2021), https://doi.org/10.1038/s43246-021-00127-0.
[45] J. Dong, Y. Huan, B. Huang, J. Yi, Y.H. Liu, B.A. Sun, W.H. Wang, H.Y. Bai, Unusually thick shear-softening surface of micrometer-size metallic glasses, Int. J. Hydrog Energ. 2 (2) (2021) 100106, https://doi.org/10.1016/j.xinn.2021.100106.
[46] Z. Huang, J. Fu, X. Li, W. Wen, H. Lin, Y. Lou, F. Luo, Z. Zhang, X. Liang, J. Ma, Ultrasonic-assisted rapid cold welding of bulk metallic glasses, Sci. China-Mater. 64 (2021) 1–8, https://doi.org/10.1007/s40843-021-1723-6.
[47] X. Li, D. Wei, J.Y. Zhang, X.D. Liu, Z. Li, T.Y. Wang, Q.F. He, Y.J. Wang, J. Ma, W. H. Wang, Y. Yang, Ultrasonic plasticity of metallic glass near room temperature, Appl. Mater. Today 21 (2020) 100866, https://doi.org/10.1016/j.apmt.2020.100866.
[48] L. Li, X. Li, Z. Huang, J. Huang, Z. Liu, J. Fu, W. Wen, Y. Zhang, S. Huang, S. Ren, J. Ma, Joining of metallic glasses in liquid via ultrasonic vibrations, Nat. Commun. 14 (1) (2023), https://doi.org/10.1038/s41467-023-42014-x.
[49] X. Li, L. Li, S. Sohrabi, J.n. Fu, Z. Li, Z. Chen, R. Sun, Y. Zhang, J. Huang, H. Zhang, Ultrasonic vibration enabled under-liquid forming of metallic glasses, Sci. Bull. 69 (2) (2024) 163–166, https://doi.org/10.1016/j.scib.2023.11.049.
[50] C. Chang, H.P. Zhang, R. Zhao, F.C. Li, P. Luo, M.Z. Li, H.Y. Bai, Liquid-like atoms in dense-packed solid glasses, Nat. Mater. 21 (11) (2022) 1240–1245, https://doi.org/10.1038/s41563-022-01327-w.
[51] Z. Chen, S. Ren, R. Zhao, J. Zhu, X. Li, H. Zhang, H. Lin, J. Zhu, S. Sohrabi, W. Ruan, J. Ma, Plasticity and rejuvenation of aged metallic glasses by ultrasonic vibrations, J. Mater. Sci. Technol. 181 (2024) 231–239, https://doi.org/10.1016/j.jmst.2023.09.029.
[52] P. Luo, Z. Lu, Y. Li, H. Bai, P. Wen, W. Wang, Probing the evolution of slow flow dynamics in metallic glasses, Phys. Rev. B 93 (10) (2016) 104204, https://doi.org/10.1103/PhysRevB.93.104204.
[53] A. Van den Beukel, J. Sietsma, The glass transition as a free volume related kinetic phenomenon, Acta Metall. Mater. 38 (3) (1990) 383–389, https://doi.org/10.1016/0956-7151(90)90142-4.
[54] R. Zhao, H. Jiang, P. Luo, L. Shen, P. Wen, Y. Sun, H. Bai, W. Wang, Reversible and irreversible β-relaxations in metallic glasses, Phys. Rev. B 101 (9) (2020) 094203, https://doi.org/10.1103/PhysRevB.101.094203.
[55] X. Guo, L. Qiu, M. Li, F. Tian, X. Ren, S. Jie, S. Geng, G. Han, Y. Huang, Y. Song, Accelerating the generation of NiOOH by in-situ surface phosphating nickel sulfide for promoting the proton-coupled electron transfer kinetics of urea electrolysis, Chem. Eng. J. 483 (2024) 149264, https://doi.org/10.1016/j.cej.2024.149264.
[56] L. He, M. Li, L. Qiu, S. Geng, Y. Liu, F. Tian, M. Luo, H. Liu, Y. Yu, W. Yang, Single-atom Mo-tailored high-entropy-alloy ultrathin nanosheets with intrinsic tensile strain enhance electrocatalysis, Nat. Commun. 15 (1) (2024) 2290, https://doi.org/10.1038/s41467-024-45874-z.
[57] B. Conway, L. Bai, Determination of adsorption of OPD H species in the cathodic hydrogen evolution reaction at Pt in relation to electrocatalysis, J. Electroanal. Chem. Interfacial Electrochem. 198 (1) (1986) 149–175, https://doi.org/10.1016/0022-0728(86)90033-1.
[58] S. Battiato, L. Bruno, A. Terrasi, S. Mirabella, Superior performances of electroless-deposited Ni–P films decorated with an ultralow content of Pt for water-splitting reactions, ACS Appl. Energy Mater. 5 (2) (2022) 2391–2399, https://doi.org/10.1021/acsaem.1c03880.
[59] X. Tian, P. Zhao, W. Sheng, Hydrogen evolution and oxidation: mechanistic studies and material advances, Adv. Mater. 31 (31) (2019) 1808066, https://doi.org/10.1002/adma.201808066Digital.
[60] C. Pei, S. Chen, T. Zhao, M. Li, Z. Cui, B. Sun, S. Hu, S. Lan, H. Hahn, T. Feng, Nanostructured metallic glass in a highly upgraded energy state contributing to efficient catalytic performance, Adv. Mater. 34 (26) (2022) 2200850, https://doi.org/10.1002/adma.202200850Digital.
[61] H. Ashassi-Sorkhabi, M. Es, Corrosion resistance enhancement of electroless Ni–P coating by incorporation of ultrasonically dispersed diamond nanoparticles, Corros. Sci. 77 (2013) 185–193, https://doi.org/10.1016/j.corsci.2013.07.046.
[62] J. Pan, Y. Wang, Q. Guo, D. Zhang, A. Greer, Y. Li, Extreme rejuvenation and softening in a bulk metallic glass, Nat. Commun. 9 (1) (2018) 1–9, https://doi.org/10.1038/s41467-018-02943-4.
[63] M. Gao, J.H. Perepezko, Mapping the viscoelastic heterogeneity at the nanoscale in metallic glasses by static force spectroscopy, Nano Lett. 20 (10) (2020) 7558–7565, https://doi.org/10.1021/acs.nanolett.0c03026.
[64] Z. Lu, W. Jiao, W. Wang, H. Bai, Flow unit perspective on room temperature homogeneous plastic deformation in metallic glasses, Phys. Rev. Lett. 113 (4) (2014) 045501, https://doi.org/10.1103/PhysRevLett.113.045501.
[65] Y. Cheng, E. Ma, Atomic-level structure and structure–property relationship in metallic glasses, Prog. Mater. Sci. 56 (4) (2011) 379–473, https://doi.org/10.1016/j.pmatsci.2010.12.002.
[66] T. Egami, Atomic level stresses, Prog. Mater. Sci. 56 (6) (2011) 637–653, https://doi.org/10.1016/j.pmatsci.2011.01.004.
[67] X. Yang, R. Liu, M. Yang, W.-H. Wang, K. Chen, Structures of local rearrangements in soft colloidal glasses, Phys. Rev. Lett. 116 (23) (2016) 238003, https://doi.org/10.1103/PhysRevLett.116.238003.
[68] H. Xu, B. Fei, G. Cai, Y. Ha, J. Liu, H. Jia, J. Zhang, M. Liu, R. Wu, Boronization-induced ultrathin 2D nanosheets with abundant crystalline–amorphous phase boundary supported on nickel foam toward efficient water splitting, Adv. Energy Mater. 10 (3) (2020) 1902714, https://doi.org/10.1002/aenm.201902714.
[69] H. Han, H. Choi, S. Mhin, Y.-R. Hong, K.M. Kim, J. Kwon, G. Ali, K.Y. Chung, M. Je, H.N. Umh, Advantageous crystalline–amorphous phase boundary for enhanced electrochemical water oxidation, Energy Environ. Sci. 12 (8) (2019) 2443–2454, https://doi.org/10.1039/C9EE00950G.
[70] L. Zhang, H. Jang, H. Liu, M.G. Kim, D. Yang, S. Liu, X. Liu, J. Cho, Sodium-decorated amorphous/crystalline RuO_2 with rich oxygen vacancies: a robust pH-

universal oxygen evolution electrocatalyst, Angew. Chem. 133 (34) (2021) 18969–18977, https://doi.org/10.1002/ange.202106631.
[71] Y. Chen, Z. Lai, X. Zhang, Z. Fan, Q. He, C. Tan, H. Zhang, Phase engineering of nanomaterials, Nature Reviews Chemistry 4 (5) (2020) 243–256, https://doi.org/10.1038/s41570-020-0173-4.
[72] S. Chen, G. Yang, S. Luo, S. Yin, J. Jia, Z. Li, S. Gao, Y. Shao, K. Yao, Unexpected high performance of Fe-based nanocrystallized ribbons for azo dye decomposition, J. Mater. Chem. A 5 (27) (2017) 14230–14240, https://doi.org/10.1039/C7TA01206C.
[73] P. Wang, J. Wang, J. Huo, W. Xu, X. Wang, G. Wang, Fast degradation of azo dye by nanocrystallized Fe-based alloys, Sci. China Phys. Mech. Astron. 60 (2017) 1–5, https://doi.org/10.1007/s11433-017-9034-5.
[74] S.X. Liang, Z. Jia, Y.J. Liu, W. Zhang, W. Wang, J. Lu, L.C. Zhang, Compelling rejuvenated catalytic performance in metallic glasses, Adv. Mater. 30 (45) (2018) 1802764, https://doi.org/10.1002/adma.201802764Digital.
[75] D. Li, Y. Qin, J. Liu, H. Zhao, Z. Sun, G. Chen, D.Y. Wu, Y. Su, S. Ding, C. Xiao, Dense crystalline–amorphous interfacial sites for enhanced electrocatalytic oxygen evolution, Adv. Funct. Mater. 32 (7) (2022) 2107056, https://doi.org/10.1002/adfm.202107056Digital.
[76] M. Fang, D. Han, W.B. Xu, Y. Shen, Y. Lu, P. Cao, S. Han, W. Xu, D. Zhu, W. Liu, Surface-guided formation of amorphous mixed-metal oxyhydroxides on ultrathin MnO_2 nanosheet arrays for efficient electrocatalytic oxygen evolution, Adv. Energy Mater. 10 (27) (2020) 2001059, https://doi.org/10.1002/aenm.202001059Digital.
[77] J. Huang, H. Sheng, R.D. Ross, J. Han, X. Wang, B. Song, S. Jin, Modifying redox properties and local bonding of Co_3O_4 by CeO_2 enhances oxygen evolution catalysis in acid, Nat. Commun. 12 (1) (2021) 3036, https://doi.org/10.1038/s41467-021-23390-8.
[78] S. Liu, Z. Zhang, K. Dastafkan, Y. Shen, C. Zhao, M. Wang, Yttrium-doped NiMo-MoO_2 heterostructure electrocatalysts for hydrogen production from alkaline seawater, Nat. Commun. 16 (1) (2025) 773, https://doi.org/10.1038/s41467-025-55856-4.
[79] J. Jiang, Z. Lu, J. Shen, T. Wada, H. Kato, M. Chen, Decoupling between calorimetric and dynamical glass transitions in high-entropy metallic glasses, Nat. Commun. 12 (1) (2021) 3843, https://doi.org/10.1038/s41467-021-24093-w.